

## VII. APPLIED PLASMA RESEARCH\*

### A. Active Plasma Systems

#### Academic and Research Staff

Prof. L. D. Smullin  
Prof. R. J. Briggs

Prof. R. R. Parker  
Prof. K. I. Thomassen

#### Graduate Students

D. S. Guttman  
F. Herba

B. R. Kusse  
R. K. Linford

J. A. Mangano  
J. A. Rome

#### 1. INTERACTION OF A SPIRALING ELECTRON BEAM WITH A PLASMA

This work has been completed by Bruce R. Kusse and a thesis, entitled "Interaction of a Spiraling Electron Beam with a Plasma," has been submitted to the Department of Electrical Engineering, M. I. T., in partial fulfillment of the requirements for the degree of Doctor of Philosophy in June 1969.

A. Bers

#### 2. STABILITY OF ELECTRON BEAMS WITH VELOCITY SHEAR

We have continued our investigation of the effects of velocity shear in unneutralized electron beams focused by an infinite longitudinal magnetic field. After our initial report was written,<sup>1</sup> we discovered that the two necessary conditions for instability of electron beams which we had presented had been previously published by E. R. Harrison,<sup>2</sup> in 1963. Unfortunately, the conclusions that Harrison drew concerning the stability of slab electron beams with linear velocity shear were erroneous because of a mistake in his treatment of Bessel functions.

Harrison's error was pointed out by Kostin and Timofeev<sup>3</sup> who also attacked the linear velocity shear problem. We have simplified the somewhat complex analysis used by Kostin and Timofeev for the case in which the beam totally fills the space between two zero-potential conducting walls, and we have also treated the case in which the walls are separated from the beam edge. In all cases, we found that an electron beam with linear velocity shear is stable.

The geometry of our problem is shown in Fig. VII-1. A slab beam, infinite in the y and z directions, contains electrons that move in the z direction with velocity  $v_z(x)$ . We assume a dependence of  $\exp[j(\omega t - kz)]$ , where k is real, and for

---

\*This work was supported by the National Science Foundation (Grant GK-10472); additional support was received from the Joint Services Electronics Programs (U.S. Army, U.S. Navy, and U.S. Air Force) under Contract DA 28-043-AMC-02536(E).

(VII. APPLIED PLASMA RESEARCH)

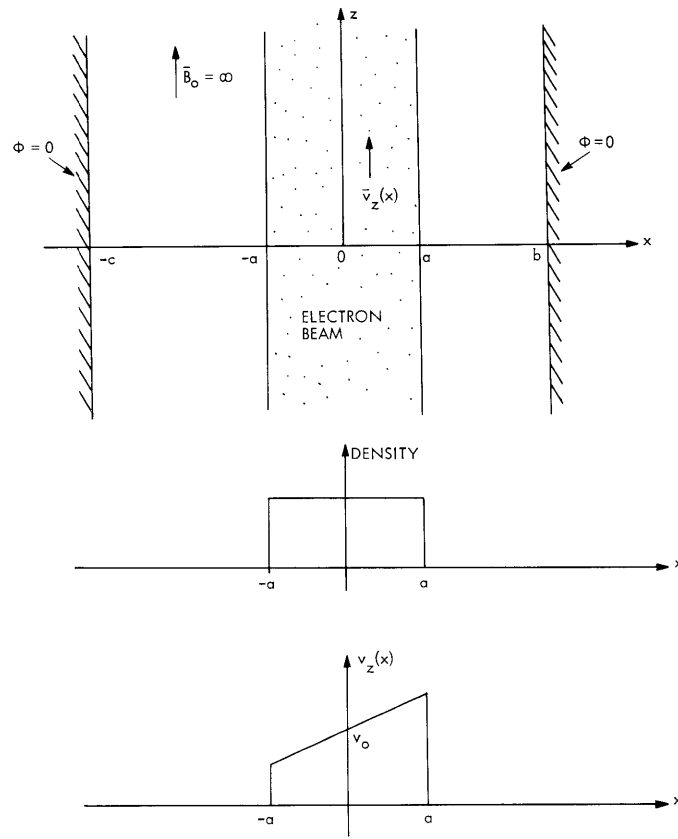


Fig. VII-1. Problem geometry.

unstable modes  $\omega \triangleq \omega_r + j\omega_i$  with  $\omega_i < 0$ . The differential equation for the linearized small-signal potential,  $\phi$ , is given by<sup>1</sup>

$$\frac{d^2\phi}{dx^2} - k^2 \left[ 1 - \frac{\omega_p^2(x)}{[\omega - kv_z(x)]^2} \right] \phi = 0. \quad (1)$$

We now consider a linear velocity profile of the form

$$v_z(x) = v_0 + ax \quad (2)$$

and make the substitution  $\phi = s^{1/2}\psi$ , where

$$s = x + \frac{v_0 - \frac{\omega}{k}}{a} \quad (3)$$

to obtain the equation

$$\frac{d^2\psi}{ds^2} + \frac{1}{s} \frac{d\psi}{ds} - \left( k^2 - \frac{\nu^2}{s^2} \right) \psi = 0. \quad (4)$$

In deriving Eq. 4 we have assumed that the beam density is uniform, and have introduced a quantity  $\nu$  defined by

$$\nu^2 = \frac{1}{4} - \left( \frac{\omega_p}{a} \right)^2. \quad (5)$$

Equation 4 is a form of Bessel's equation, which has the solution

$$\phi = As^{1/2} [BJ_\nu(jks) + J_{-\nu}(jks)], \quad (6)$$

where A and B are arbitrary constants, to be determined by the boundary conditions.

It is interesting to note that  $\nu$  will be real if  $2\omega_p < a$ , which was one of the necessary conditions for instability. Conversely,  $\nu$  will be pure imaginary if  $2\omega_p > a$ . This causes a fundamental change in the nature of the solutions as the slope of the velocity profile is varied about the value  $2\omega_p$ .

#### CASE I: Walls at the Edge of the Beam ( $x = \pm a$ )

In this case,  $\phi = 0$  at  $x = \pm a$ . If we are looking for unstable solutions,  $s$  must be complex and hence  $s^{1/2} \neq 0$ . Therefore, application of the boundary conditions leads to the determinantal equation

$$\left[ \frac{-J_{-\nu}(z)}{J_\nu(z)} \right]_{x=a} = \left[ \frac{-J_{-\nu}(z)}{J_\nu(z)} \right]_{x=-a}, \quad (7)$$

where

$$z \equiv jks = jk \left( x + \frac{v_0 - \frac{\omega_r}{k}}{a} + \frac{\omega_i}{a} \right).$$

To determine whether or not there are complex eigenvalues ( $\omega(k)$ ) that satisfy Eq. 7, we shall use a method similar to the one employed by Kostin and Timofeev.<sup>3</sup> If we introduce a function  $C(z) = -J_{-\nu}(z)/J_\nu(z)$ , then the determinantal equation requires  $C(x=a) = C(x=-a)$ . Consider a mapping of the complex  $z$ -plane onto the complex  $C$ -plane. For a fixed  $\omega_i < 0$ , as we move from  $x = -a$  to  $x = +a$ , the complex variable  $z$  will trace the path shown in Fig. VII-2. For instability,  $z(a)$  and  $z(-a)$  must lie on opposite sides of the  $z_r$  axis, because of the necessary<sup>1</sup> condition that  $v_z(x) = \omega_r/k$  somewhere in the region  $-a < x < a$ .

(VII. APPLIED PLASMA RESEARCH)

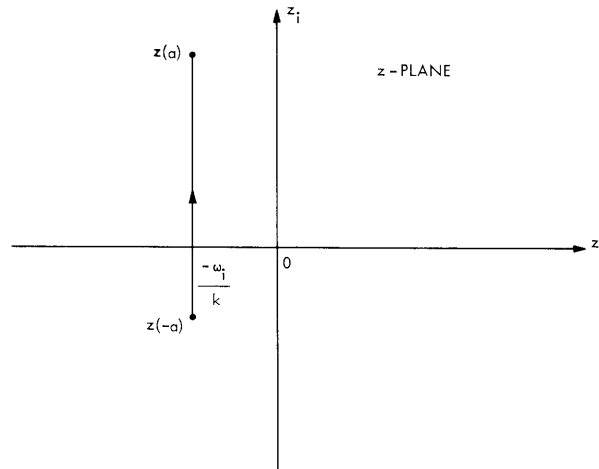


Fig. VII-2. Path of complex variable  $z$ .

Since  $z_i = \text{constant}$  for fixed  $\omega$ , the contour can only cross the  $z_r$  axis once.

This path must, however, map onto a closed contour in the C-plane if  $\omega$  is to be an eigenvalue. Thus the contour in the C-plane must be of the form shown in Fig. VII-3. This is impossible, since (as is proved in the Appendix) C is real if and only if  $z$  is real. Thus  $C(-a)$  and  $C(a)$  must be complex as shown in the figure. This forces the

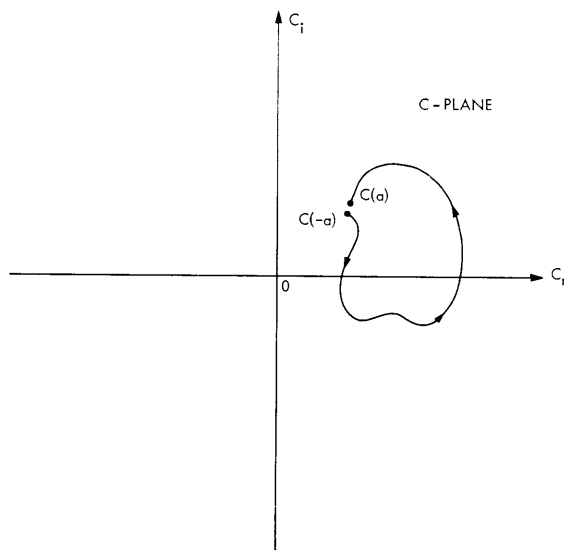


Fig. VII-3. Contour in C-plane.

C-contour to cut the  $C_r$  axis an even number of times. This is impossible because one and only one real point on the C-contour must correspond to the single real point on the z-contour.

Therefore it is impossible to satisfy the boundary conditions for complex  $\omega$ , and hence the beam is stable.

The question now arises whether any solutions for real  $\omega$  exist. If  $v^2 > 0$ , a similar argument shows that only two neutral modes exist, with phase velocities corresponding to the beam velocity at the edges.

For the case  $v^2 < 0$ , let  $v = j\rho$ . We now have

$$C(z) = \frac{J_{-j\rho}(z)}{J_{j\rho}(z)}, \quad (8)$$

where now  $z$  will have to be pure imaginary for a neutral eigenvalue. Let  $z = +jy$ . Using the power series expansion of the Bessel functions, we get

$$C(jy) = -e^{\rho\pi} \exp\left[-2j\rho \log \left|\frac{1}{2}y\right|\right] \exp\left\{2j \operatorname{Arg} \left[ \sum_{m=0}^{\infty} \frac{\left(\frac{1}{2}y\right)^{2m}}{m! \Gamma(-j\rho+m+1)} \right]\right\}. \quad (9)$$

As  $y$  varies through positive values,  $C(jy)$  is a circle, and hence assumes the same value an infinite number of times and thus an infinite number of (space-charge wave) modes is possible.

#### CASE II: Walls Separated from Beam Edge

If the zero-potential walls are separated from the beam edge, Eq. 1 can easily be solved in the region between the beam and the wall, since  $\omega_p \equiv 0$ . The solution in this region yields a constraint on  $\phi'/\phi$  at each edge of the beam. If the walls are at infinity,

$$\frac{\phi'}{\phi} = \mp k \quad \text{at } x = \pm a.$$

If the walls are  $+b$  and  $-c$ ,

$$\frac{\phi'}{\phi} = -k \coth k(b-a) \quad \text{at } x = +a$$

$$\frac{\phi'}{\phi} = +k \coth k(c-a) \quad \text{at } x = -a.$$

In each case,  $\phi'/\phi$  has the sign opposite to that of  $x$  at the beam edge.

Returning to Eq. 1, multiplying by  $\phi^*$ , and integrating by parts, we obtain the relation

## (VII. APPLIED PLASMA RESEARCH)

$$\phi^* \phi' \Big|_{x=a} = \phi^* \phi' \Big|_{x=-a} + \int_{-a}^a |\phi'|^2 dx + \int_{-a}^a k^2 |\phi|^2 \left[ 1 - \frac{\omega_p^2}{(\omega - kv_z)^2} \right] dx. \quad (10)$$

In general,  $\phi^* \phi' \Big|_{x=a}$  is complex, even for real  $\omega$ , because of the singular nature of the last integral. This must be carefully evaluated by taking the limit  $\omega_i \rightarrow 0$  (from below) for unstable modes.

If we know  $\phi(\omega, k, x)$  and use the known positive real value of  $\phi'/\phi$  at  $x = -a$ , we could integrate Eq. 10 numerically. If we had picked an  $\omega$  that is an eigenvalue,  $\phi^* \phi' \Big|_{x=a}$  calculated according to Eq. 10 would be a negative real number.

By our necessary condition for instability,<sup>1</sup> any unstable eigenmode must occur such that

$$kv_1 < \omega_r < kv_2, \quad (11)$$

where  $v_1$  and  $v_2$  are the minimum and maximum electron velocities, respectively. We now make the plausible assumption that as the velocity shear is reduced, an unstable eigenmode must approach a neutral eigenmode in a continuous manner such that, for the neutral modes,  $kv_1 \leq \omega \leq kv_2$ . Thus, we adopt as our necessary and sufficient condition for an unstable eigenmode that there must be a neutral eigenmode that occurs for some value of the velocity shear  $> 2\omega_p$  and for  $kv_1 \leq \omega \leq kv_2$ . For a linear velocity profile, we can show that  $\phi^* \phi' \Big|_{x=a}$  cannot be negative in this range, and hence the neutral eigenmode cannot exist.

For a monotonic velocity profile, there can only be one singular point, that is, one point where  $v(x) = \omega_r/k$ . By changing the upper or lower integration limit in Eq. 10 to  $x$ , and knowing that  $\phi^* \phi'$  is real at each beam edge, it is clear that for real  $\omega$ ,  $\phi^* \phi'$  must be real from  $x = -a$  up to the singular point and from the singular point to  $x = +a$ . Thus, for a monotonic profile, the imaginary part arising from the singular integral at the critical point must be zero.

For  $\omega$  real, and a linear velocity profile, near the singular point,  $\phi$  is approximately given by

$$\phi = As^{1/2+\nu} + Bs^{1/2-\nu}. \quad (12)$$

To make  $\phi^* \phi'$  real for real  $\omega$  in the vicinity of the critical point,  $\text{Arg}(A) = \text{Arg}(B)$ . To the right of the singular point,  $\phi'/\phi$  is given by

$$\frac{\phi'}{\phi} = \frac{\left[ \nu + \frac{1}{2} \right]}{s} \left[ \frac{1 + \frac{B}{A} \left[ \frac{\frac{1}{2} - \nu}{\frac{1}{2} + \nu} \right] e^{2\nu \ln(s)}}{1 + \frac{B}{A} e^{2\nu \ln(s)}} \right]. \quad (13)$$

On the left of the singular point,  $s$  becomes  $s e^{-j\pi}$  and  $\phi'/\phi$  becomes

$$\frac{\phi'}{\phi} = \frac{\left[ \nu + \frac{1}{2} \right]}{s e^{-j\pi}} \left[ \frac{1 + \frac{B}{A} \left[ \frac{\frac{1}{2} - \nu}{\frac{1}{2} + \nu} \right] e^{2\nu[\ln(s) - j\pi]}}{1 + \frac{B}{A} e^{2\nu[\ln(s) - j\pi]}} \right]. \quad (14)$$

The imaginary part of this is given by

$$\text{Im} \left[ \frac{\phi'}{\phi} \right] = \frac{-\left[ \nu + \frac{1}{2} \right]}{s} \frac{\left[ \frac{2\nu}{\nu + \frac{1}{2}} \right] e^{2\nu \ln(s)} \sin(2\nu\pi)}{1 + \left( \frac{B}{A} \right)^2 e^{4\nu \ln(s)} + 2 \left( \frac{B}{A} \right) e^{2\nu \ln(s)} \cos(2\nu\pi)}. \quad (15)$$

If  $\nu > 0$ , this equation is only zero if  $\frac{B}{A} \rightarrow 0$  or  $\frac{B}{A} \rightarrow \infty$ . Thus either  $A = 0$  or  $B = 0$ , and only one of the two independent solutions to the differential equation (1) can be used.

Therefore, for the case at hand,

$$\phi = A s^{1/2} J_{\pm\nu}(jks), \quad (16)$$

where either the plus sign or the minus sign must be used, but not a linear combination of the two. Using the series expansions for the Bessel functions,

$$\frac{\phi'}{\phi} = \frac{1}{2s} + \frac{1}{s} \left\{ \frac{\sum_{n=0}^{\infty} \frac{\left( \frac{1}{2} ks \right)^{\pm\nu+2n}}{n! \Gamma(\pm\nu+n+1)}}{\sum_{m=0}^{\infty} \frac{\left( \frac{1}{2} ks \right)^{\pm\nu+2m}}{m! \Gamma(\pm\nu+m+1)}} + \frac{\sum_{n=0}^{\infty} \frac{2n \left( \frac{1}{2} ks \right)^{\pm\nu+2n}}{n! \Gamma(\pm\nu+n+1)}}{\sum_{m=0}^{\infty} \frac{\left( \frac{1}{2} ks \right)^{\pm\nu+2m}}{m! \Gamma(\pm\nu+m+1)}} \right\} \quad (17)$$

or,

$$\frac{\phi'}{\phi} = \frac{1}{s} \left( \frac{1}{2} \pm \nu \right) + \frac{1}{s} \left\{ \frac{\sum_{n=0}^{\infty} \frac{2n \left( \frac{1}{2} ks \right)^{\pm\nu+2n}}{n! \Gamma(\pm\nu+n+1)}}{\sum_{m=0}^{\infty} \frac{\left( \frac{1}{2} ks \right)^{\pm\nu+2m}}{m! \Gamma(\pm\nu+m+1)}} \right\}. \quad (18)$$

The term in braces is  $\geq 0$  for  $k > 0$ . Since  $0 < \nu < 1/2$ , the right-hand side of Eq. 18

## (VII. APPLIED PLASMA RESEARCH)

has the same sign as  $s$  and the sign of  $s$  is the same as that of  $x$ . Thus  $\phi'/\phi$  is always positive at  $x = +a$ , and so is  $\phi^* \phi'$ . This is a contradiction to the boundary conditions, and thus there can be no unstable solutions.

In conclusion, we have shown that no matter where the zero-potential walls are located, slab electron beams with linear velocities shear are stable.

### Appendix

We shall prove that  $C(z) = \frac{-J_{-\nu}(z)}{J_{\nu}(z)}$  is real if and only if  $z$  is real. From the power-series expansion for  $J_{\pm\nu}(z)$ , it is obvious that if  $z$  is real, both  $J_{\nu}(z)$  and  $J_{-\nu}(z)$  are real if we are careful to use the same sheet for each Bessel function. Hence  $C(z)$  will be real.

It is harder to show that if  $z$  is complex, then  $C(z)$  is also complex. It is well known that the zeros of  $J_{\nu}(z)$  and  $J_{-\nu}(z)$  only occur for  $z$  real. Thus the zeros of  $C(z)$  coincide with the zeros of  $J_{-\nu}(z)$  and are real. Suppose there exists a complex  $z_0$ , which corresponds to a real  $C(z)$ ,  $C(z_0)$ . Since  $C(z)$  is analytic for complex  $z$ , a neighborhood of  $z_0$  must map onto a neighborhood of  $C(z_0)$  which is real. Thus other points that neighbor  $z_0$  must map onto the real  $C$  axis. Thus there exists a contour in the complex  $z$ -plane which will map onto the real  $C$  axis. In particular, some point on this contour must map onto the point  $C = 0$ , and hence this contour must pass through one of the real zeros of  $J_{-\nu}(z)$ ,  $z_1$ . Since at least two contours that pass through  $C$  map onto the real  $C$  axis,  $z_1$  must be a branch point which implies

$$\frac{dz}{dC} = \frac{\pi z J_{\nu}^2(z)}{\sin \pi \nu} = 0.$$

Zeros of  $dz/dC$  only occur, however, at the zeros of  $J_{\nu}(z)$  that do not correspond to the zeros of  $J_{-\nu}(z)$ , hence  $z_1$  cannot be a branch point and, therefore,  $z_0$  cannot be complex.

J. A. Rome, R. J. Briggs

### References

1. R. J. Briggs and J. A. Rome, "Stability of Electron Beams with Velocity Shear," Quarterly Progress Report No. 90, Research Laboratory of Electronics, M. I. T., July 15, 1968, pp. 106-107.
2. E. R. Harrison, "Longitudinal Electrostatic Oscillations in Velocity Gradient Plasmas I. The Slipping-Stream Model," Proc. Phys. Soc. (London) 82, 689-699 (1963).
3. V. M. Kostin and A. V. Timofeev, "Stability of an Electron Current with a Velocity Gradient," Soviet Phys. - JETP 26, 801-805 (April 1968).



## VII. APPLIED PLASMA RESEARCH\*

### B. Plasma Effects in Solids

#### Academic Research Staff

Prof. G. Bekefi  
Prof. G. A. Baraff

#### Graduate Students

E. V. George  
C. S. Hartmann

D. A. Platts  
R. N. Wallace

### 1. ACOUSTIC-WAVE PROPAGATION AND AMPLIFICATION IN InSb

In a previous report<sup>1</sup> we described the acoustic-wave propagation characteristics in InSb and the relevant elastic and piezoelectric parameters that enter into the gain formulation given in other reports.<sup>2,3</sup> In this report, we describe the acoustic-wave propagation characteristics in an arbitrary crystallographic direction. By using crystal symmetry properties and extrapolating our computed results, we can approximately describe the acoustic-wave propagation characteristics for an arbitrary direction of propagation in InSb. A detailed development of the equations that were used may be found in our previous report<sup>1</sup> and in a recently completed Master's thesis.<sup>4</sup> For the sake of brevity, these equations are omitted here.

Because of the symmetry of InSb,<sup>5</sup> we need consider only 1/48 of all possible directions of wave propagation. Figure VII-4a shows one octant of space divided into 6 equivalent regions. In this figure spatial directions are indicated by points on the surface of a sphere. The direction is given by the radius vector to that point. The  $x_1$ ,  $x_2$ , and  $x_3$  axes are the principal axes of the cubic crystal InSb. The three arcs (AB, BG, and DG) shown in Fig. VII-4b indicate the directions for which the equations were solved. By using crystal-symmetry arguments, one can draw these same axes through equivalent points in one of these regions, as shown in Fig. VII-4c. Note that this choice of directions gives the solutions for the entire boundary of each symmetrical region, and for a whole series of directions inside each region. The graphs that follow will be labeled in terms of the angles  $\theta$  and  $\phi$ , which are defined in Fig. VII-5. In this figure,  $\bar{q}$  is the acoustic propagation vector.

Figure VII-6 shows the propagation velocities for all three modes for the paths AB and BCG shown in Fig. VII-4b. Note that the segment CG is equivalent to CA in Fig. VII-4c. Figure VII-7 shows the velocities for the path DG of Fig. VII-4b. This is equivalent to the path DFEA in Fig. VII-4c.

The acoustic-wave velocity is only one of the parameters that we need to know

---

\*This work was supported by the National Science Foundation (Grant GK-10472).

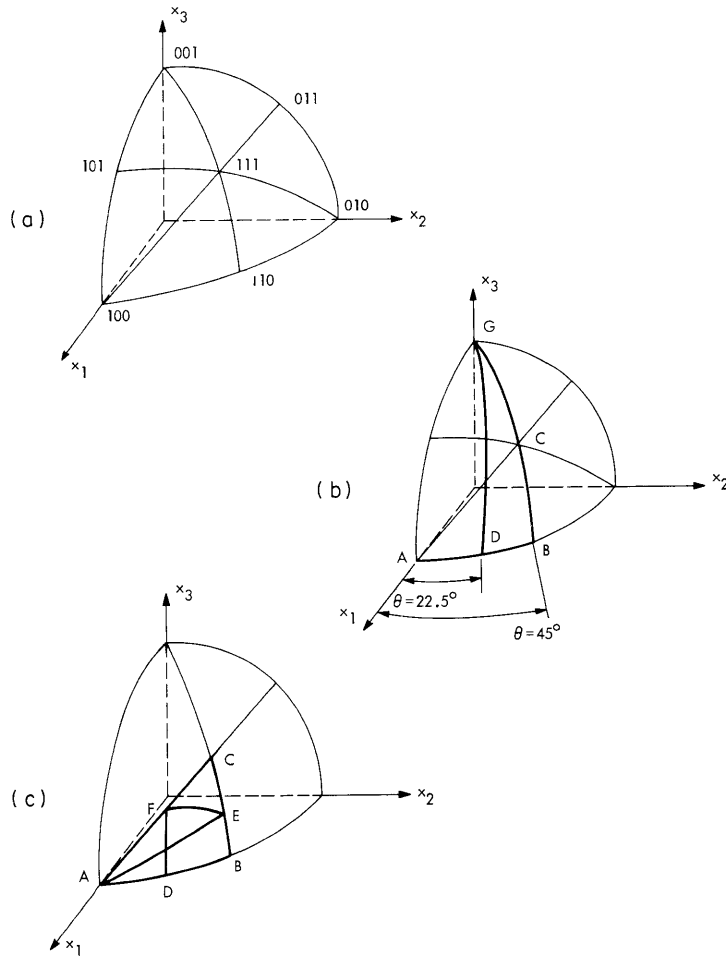


Fig. VII-4. Directions of wave propagation considered here.

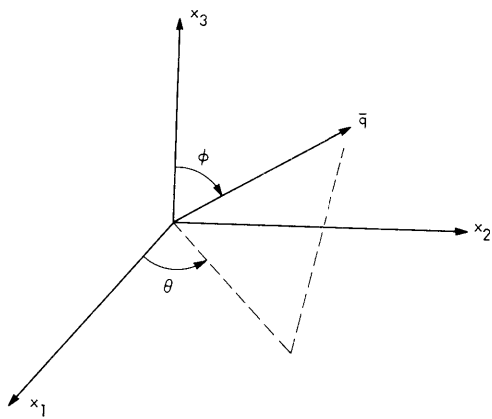


Fig. VII-5. Directions of wave propagation considered here.

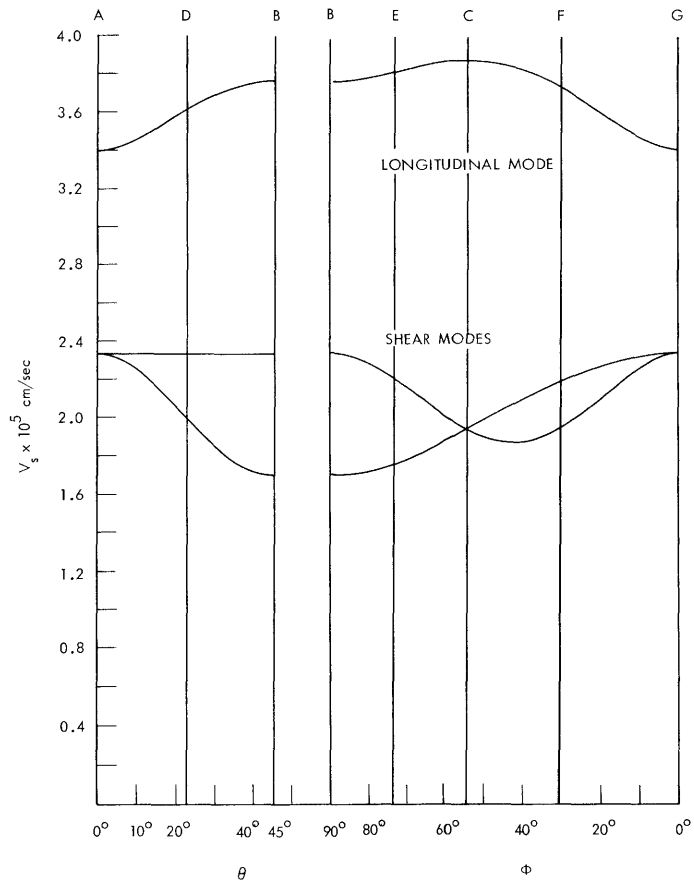


Fig. VII-6. Propagation velocities for all three modes in InSb as a function of the direction of  $q$ .

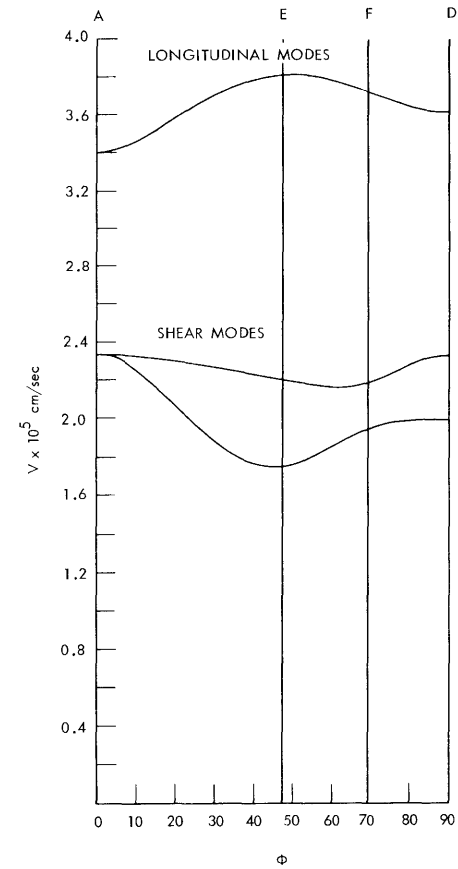


Fig. VII-7. Propagation velocities for all three modes in InSb as a function of the direction of  $q$ .

(VII. APPLIED PLASMA RESEARCH)

to calculate the acoustic gain. The other parameter is the longitudinal effective piezoelectric coefficient  $e_p$ , which is defined by Eq. 8 in the previous report.<sup>1</sup> This constant gives the magnitude of the coupling between an acoustic wave and an electric field that is parallel to the direction of wave propagation. Figure VII-8 shows  $e_p$  for the paths AB and BCG of Fig. VII-4b. The same crystal symmetry arguments apply, and thus the path CG is equivalent to CA in Fig. VII-4c. Figure VII-9 shows  $e_p$  for the path DG of Fig. VII-4b. This is equivalent to the path DFEA in Fig. VII-4c. The ordinates of Figs. VII-8 and VII-9 are given in terms of  $e_p/e_{14}$  ( $e_{14}$  is the single nonvanishing piezoelectric constant in the piezoelectric tensor for a cubic material such as InSb). Nill<sup>6</sup> has measured this constant for InSb and found it to be  $0.06 \text{ C/m}^2$ .

As discussed in the previous report,<sup>1</sup> the elastic properties enter differently into the maximum gain expression for different frequency regimes. In this report, we shall give the calculations for the growth constant at the frequency of maximum gain. Figures VII-10, VII-11, and VII-12 show contours of constant  $e_p^2/e_{14}^2 V_s^2$  for the longitudinal, fast transverse, and slow transverse modes, respectively. These figures are drawn on a stereographic projection of a sphere. We note that each mode has a peak with respect to the direction of propagation. In a previous report,<sup>3</sup> the maximum gain is calculated under the assumptions that  $e_p = e_{14}$  and  $V_s = 4 \times 10^3 \text{ m/sec}$ . If we use our values for  $e_p$  and  $V_s$  in the maximum gain equation, we obtain the following values at the peak for each mode. Note that the peak for the

Mode	Angle Coordinates of Peak		Crystallographic Direction	$\frac{e_p}{e_{14}}$	$V_s$ (km/sec)	Max Gain (dB/cm)
	$\theta$	$\phi$				
Longitudinal	$45^\circ$	$54.8^\circ$	111	1.15	3.87	27
Fast transverse	$45^\circ$	$90^\circ$	110	1.0	2.33	56
Slow transverse	$\sim 22.5^\circ$	$\sim 69^\circ$	—	.53	1.95	23

slow shear mode does not occur along one of the high-symmetry axes of the crystal.

Several points should be emphasized. (i) These figures show the maximum possible gain for any given direction of propagation. This maximum gain will only occur if the DC electric and magnetic fields have the proper magnitude and direction. (ii) We cannot maximize the gain for all directions of propagation simultaneously. For example, suppose we have applied the proper fields to maximize the gain in the [110] direction. With these fields applied to the sample, the gain in the

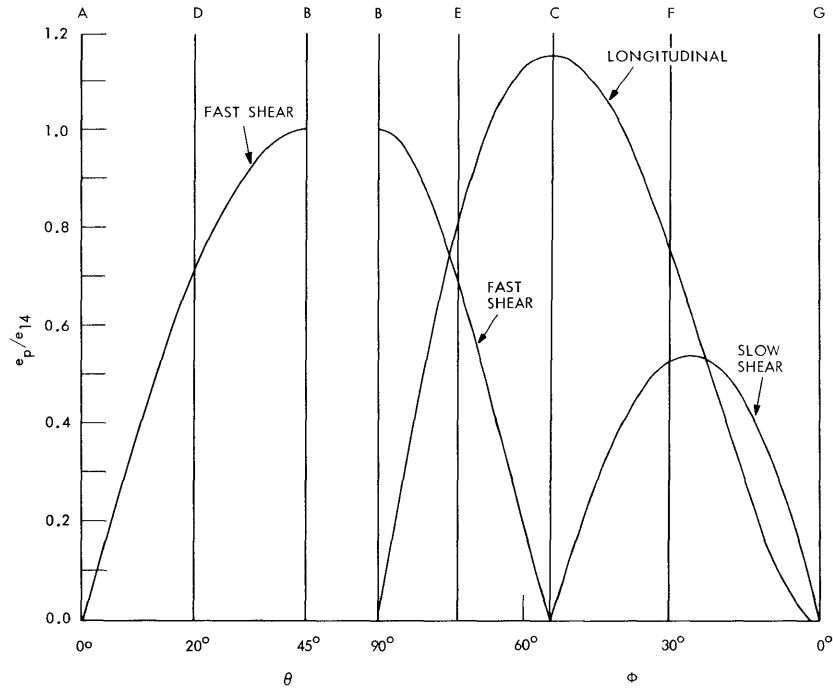


Fig. VII-8. Longitudinal effective piezoelectric constant as a function of the direction of  $q$ .

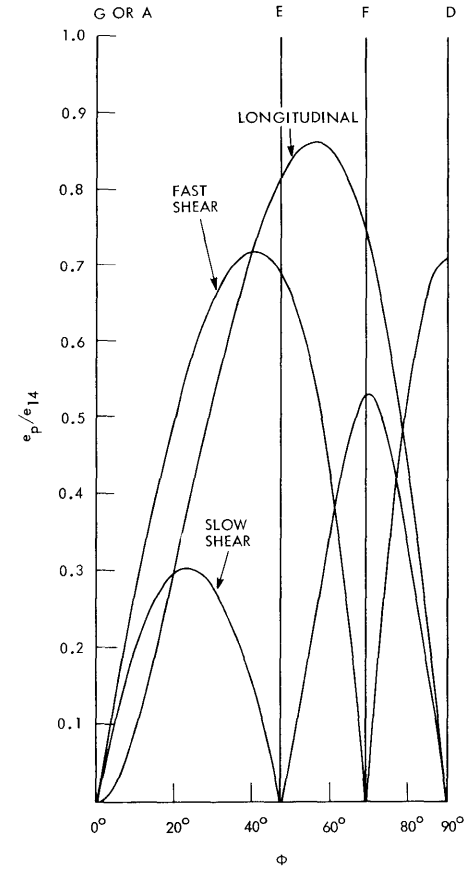


Fig. VII-9. Longitudinal effective piezoelectric constant as a function of the direction of  $q$ .

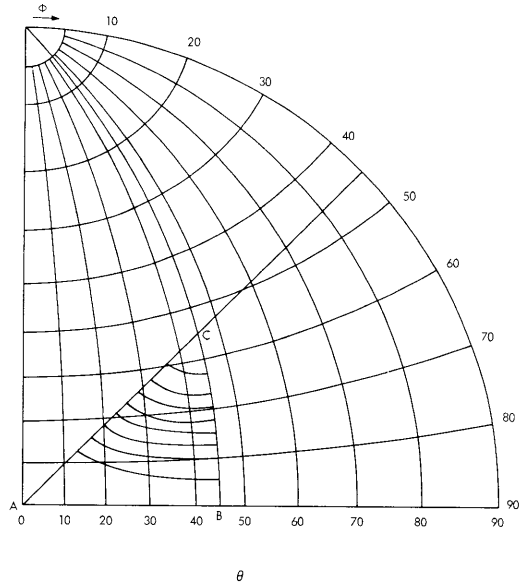


Fig. VII-10. Contours of equal maximum gain for the longitudinal mode. Each step corresponds to 3.1 dB.

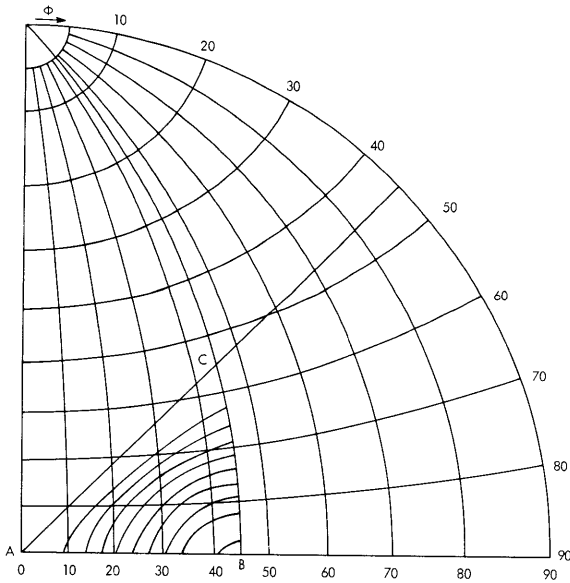


Fig. VII-11. Contours of equal maximum gain for the fast transverse mode. Each step corresponds to 6.2 dB.

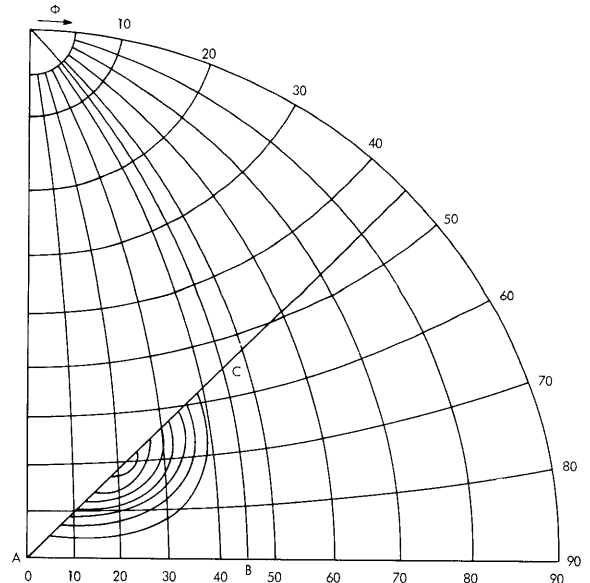


Fig. VII-12. Contours of equal maximum gain for the slow transverse mode. Each step corresponds to 3.1 dB.

## (VII. APPLIED PLASMA RESEARCH)

[111] direction will not in general be maximized. (iii) These contours are proportional to  $q_1$  which enters the wave solution as on  $e^{q_1 x}$  growth factor. This means that these curves are directly proportional to the maximum gain in dB/cm. For example, if we investigate the maximum gain at a contour corresponding to 1/2 the peak value for that mode, this maximum gain is not 3 dB down from the peak value. The gain is the peak value gain in dB/cm divided by 2.

Similar contour plots can be made for other frequency regimes ( $\omega \gtrsim \omega_{\max}$ ) by using the information given in Figs. VII-6 through VII-9. In all cases, however, the maximum possible gain occurs for the fast shear wave propagation in the [110] direction.

C. S. Hartmann, A. Bers

### References

1. C. S. Hartmann and A. Bers, Quarterly Progress Report No. 90, Research Laboratory of Electronics, M. I. T., July 15, 1968, pp. 118-124.
2. A. Bers, Quarterly Progress Report No. 88, Research Laboratory of Electronics, M. I. T., January 15, 1968, pp. 204-209.
3. D. A. Platts and A. Bers, Quarterly Progress Report No. 89, Research Laboratory of Electronics, M. I. T., April 15, 1968, pp. 164-167.
4. C. S. Hartmann, S.M. Thesis, Department of Electrical Engineering, M. I. T., August 1968.
5. W. P. Mason, Piezoelectric Crystals and Their Application to Ultrasonics (D. Van Nostrand Company, Inc., New York, 1950).
6. K. W. Nill, Ph.D. Thesis, Department of Electrical Engineering, M. I. T., May 1966.

## VII. APPLIED PLASMA RESEARCH\*

### C. Plasma Physics and Engineering

#### Academic and Research Staff

Prof. D. J. Rose  
Prof. T. H. Dupree

Prof. E. P. Gyftopoulos  
Prof. L. M. Lidsky

Prof. W. M. Manheimer  
Dr. R. A. Blanken

#### Graduate Students

N. M. Ceglio  
H. Ching  
D. G. Colombant

M. Hudis  
T. R. Hulick  
M. A. Lecomte  
G. R. Odette

K. Ohmae  
C. E. Wagner  
R. J. Vale

### 1. ELECTRON-CYCLOTRON RESONANCE-HEATED PLASMA IN A LEVITRON

We are reporting on the preliminary results of an investigation of the diffusion of an electron-cyclotron resonance-heated plasma in a levitron. Heating is achieved by using 1-MW, 10- $\mu$ sec pulses of microwaves of  $\sim 2.8$  GHz (S-band) from a Bendix klystron radar transmitter LL-KRX-3 with a Raytheon QK327 magnetron. The magnetic field is produced by discharging capacitor banks into the poloidal magnet, a circular coil, and the toroidal magnet, a longitudinal bar, as in Fig. VII-13. The magnetic field

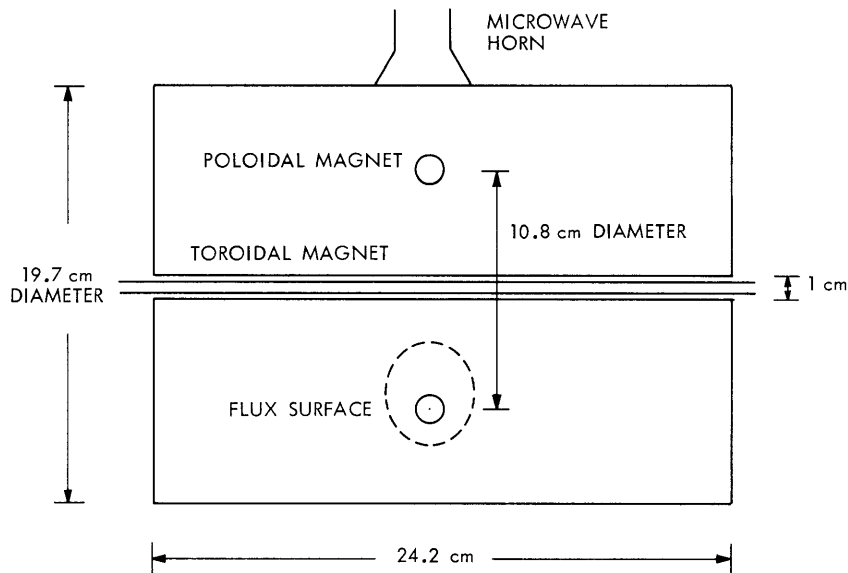


Fig. VII-13. Magnet coil arrangement in plasma chamber.

\*This work was supported by the National Science Foundation (Grant GK-10472); additional support was received from the Joint Services Electronics Programs (U.S. Army, U.S. Navy, and U.S. Air Force) under Contract DA 28-043-AMC-02536(E).



decays less than 3% during the lifetime of the plasma. Resonance heating occurs on the 1-kG surface, forming a torus around the poloidal magnet. The toroidal magnet provides shear. This magnetic configuration was predicted by Lehnert<sup>1</sup> to be exceptionally stable. Kuckes and Turner<sup>2</sup> at Culham Laboratory have found that the loss rate from their levitron was an order of magnitude slower than that predicted by Bohm diffusion.

Preliminary measurements have been made with hydrogen at pressures of the order of  $10^{-4}$  Torr, using a phototube and a spherical Langmuir probe. Our findings indicate an electron temperature of  $\sim 5$  eV, with a density of  $\sim 10^{11}/\text{cm}^3$  in a plasma lasting approximately 50  $\mu\text{sec}$ . Oscillations were observed in both phototube and probe ion saturation measurements with a well-defined frequency varying between 120 kHz and 140 kHz. Kuckes and Turner have noted potential fluctuations at a well-defined frequency that varied between 50 kHz and 200 kHz. Crude calculations indicate diffusion several times slower than Bohm diffusion.

We are continuing to study the diffusion and low-frequency oscillation of the plasma.

A. S. Ratner, R. A. Blanken

#### References

1. B. Lehnert, "On the Confinement of Charged Particles in a Magnetic Field," J. Nucl. Energy C1, 40 (1959).
2. A. F. Kuckes and R. B. Turner, "Plasma Confinement and Potential Fluctuation in a Small Aspect Ratio Levitron," IAEC: Third Conference on Plasma Physics and Controlled Nuclear Fusion Research, Novosibirsk, U.S.S.R., August 1968.

#### 2. GAIN OF A CO<sub>2</sub> LASER AMPLIFIER IN THE AFTERGLOW

Physical reasons that are best described by Fig. VII-22 led us to expect that a pulsed CO<sub>2</sub>-He-N<sub>2</sub> laser might be more efficient in the afterglow. In order to verify this expectation, we measured experimentally the gain of a CO<sub>2</sub>-He-N<sub>2</sub> amplifier under various conditions – changing gas pressures and current – in the glow and in the afterglow. A Q-switched CO<sub>2</sub> laser supplied the probe pulses ( $\sim 300$  nsec).

Indeed, we found a gain increment in the afterglow. The best measured gain was 2.4/m.

#### Experimental Arrangement and Procedure

Figure VII-14 shows the experimental arrangement. The 35-cm amplifier is excited by a pulse generated by a timing device driving a high-voltage power supply (5000 V). The purpose of this timing device is to pulse the DC power supply of the amplifier so that the test pulse from the laser can be sent through the amplifier at will, at any time during the excitation or in the afterglow (see Figs. VII-15 and VII-16). Two oscilloscopes

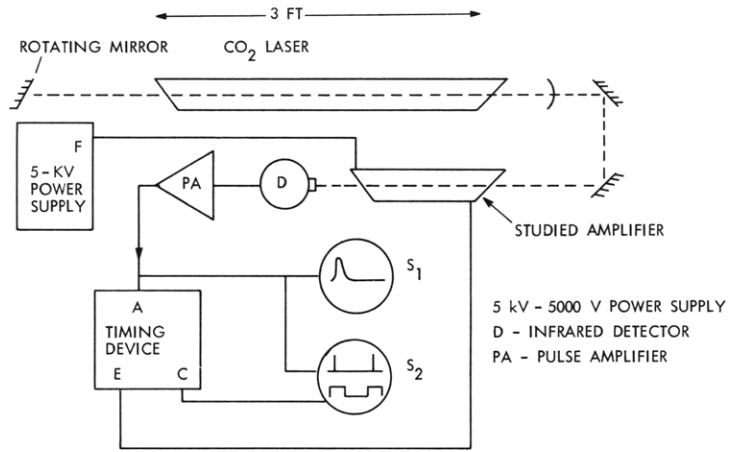


Fig. VII-14. Experimental arrangement.

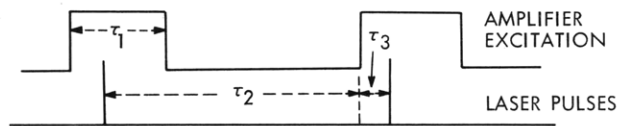
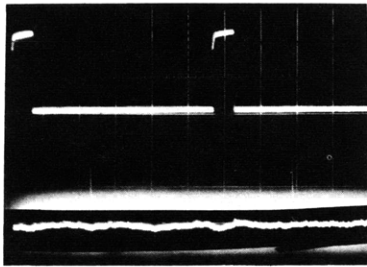
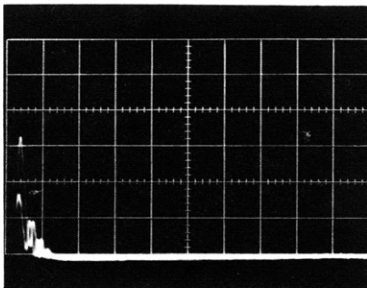


Fig. VII-15. Diagram of the timing device.



(a)



(b)

Fig. VII-16. S<sub>1</sub> and S<sub>2</sub> oscilloscope displays showing evidence of the amplifier gain.

permit watching the variation of the test pulse magnitude as a function of the time or of the gas mixture. The laser is Q-switched at a rate of 60 Hz. Its very short pulse is used to probe the amplifier and to drive the timing device so that the amplifier excitation is synchronized with the rotating mirror. A delay included in the timing device allows us to vary  $\tau_3$  (Fig. VII-15) whenever we wish, and observation of both oscilloscopes  $S_1$  (Fig. VII-16b) and  $S_2$  (Fig. VII-16a) yields the amplitude variation of the test pulse and  $\tau_3$ .

### Experimental Results

Figure VII-16b illustrates the observation of the gain, since it is, in fact, a superposition of two pictures. One picture was taken when the amplifier was not turned on (yielding the small pulse), the other one in the afterglow of the excitation of the amplifier. A gain of 2 was observed in this particular case. Let us call  $G = (E - E_0)/E_0$ , where  $E_0$  is the amplitude of the pulse when the amplifier is turned off, and  $E$  is the amplitude as the amplifier is excited. We have plotted the variations of  $G$  as a function of  $\tau_3$  for the following mixtures.

$$\left. \begin{array}{l} \text{He} = 4 \text{ Torr} \\ \text{N}_2 = 1 \text{ Torr} \\ \text{CO}_2 = \text{variable} \end{array} \right\} \text{Fig. VII-17} \quad \text{and} \quad \left. \begin{array}{l} \text{He} = 4.5 \text{ Torr} \\ \text{N}_2 = 1.5 \text{ Torr} \\ \text{CO}_2 = \text{variable} \end{array} \right\} \text{Fig. VII-18}$$

When  $G$  goes to zero, it means that the gain was too small to be observed, but, of course,  $G$  has a small positive value because a steady-state  $\text{CO}_2$  laser is a reality.

Following these measurements, we wished to see the influence of the different gases on the gain, and we plotted in Fig. VII-19 the variation of the largest  $G$  as one of each of the gas pressures was varied. In each of these experiments the excitation time  $\tau_1$  was kept constant (equal to 3 msec). Moreover, since helium may be important in the de-excitation of the lower  $\text{CO}_2$  laser level, we also plotted the variation of the time of occurrence of the largest  $G$  with the partial pressure (Fig. VII-20).

Since we expected to get a larger gain in the afterglow, the previous experimental results led us to observe the variation of the gain under the following conditions.

$$\begin{array}{ll} \text{He} & 2.5 \text{ Torr} & \text{current } 160 \text{ mA} \\ \text{CO}_2 & 2 \text{ Torr} & \text{excitation time } 0.5 \text{ msec} \\ \text{N}_2 & 1 \text{ Torr} & \end{array}$$

When the current of the amplifier was changed from 40 mA to 200 mA no significant

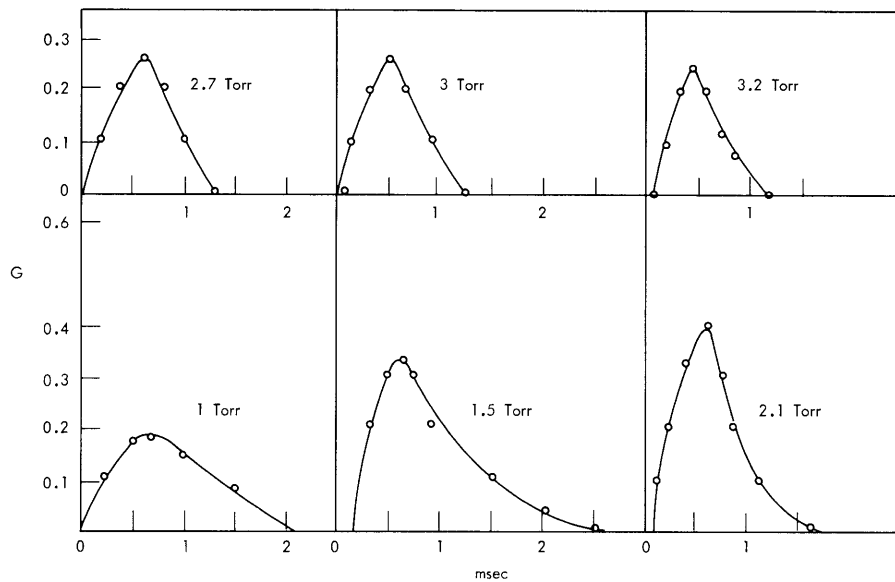


Fig. VII-17. Variation of gain with time as  $\text{CO}_2$  pressure is varied.  
He pressure, 4 Torr;  $\text{N}_2$  pressure, 1 Torr.

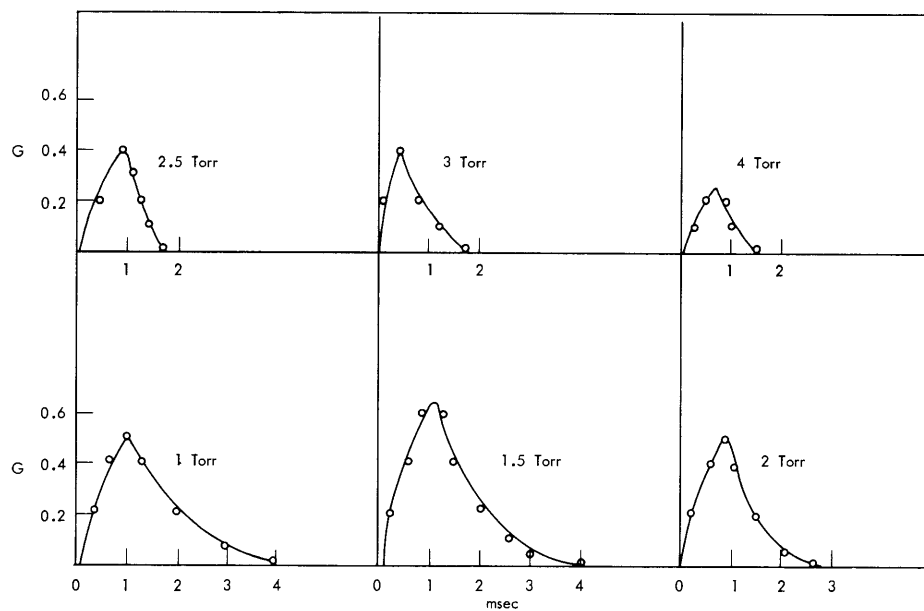


Fig. VII-18. Variation of gain with time as  $\text{CO}_2$  pressure is varied.  
He pressure, 4.5 Torr;  $\text{N}_2$  pressure, 1.5 Torr.

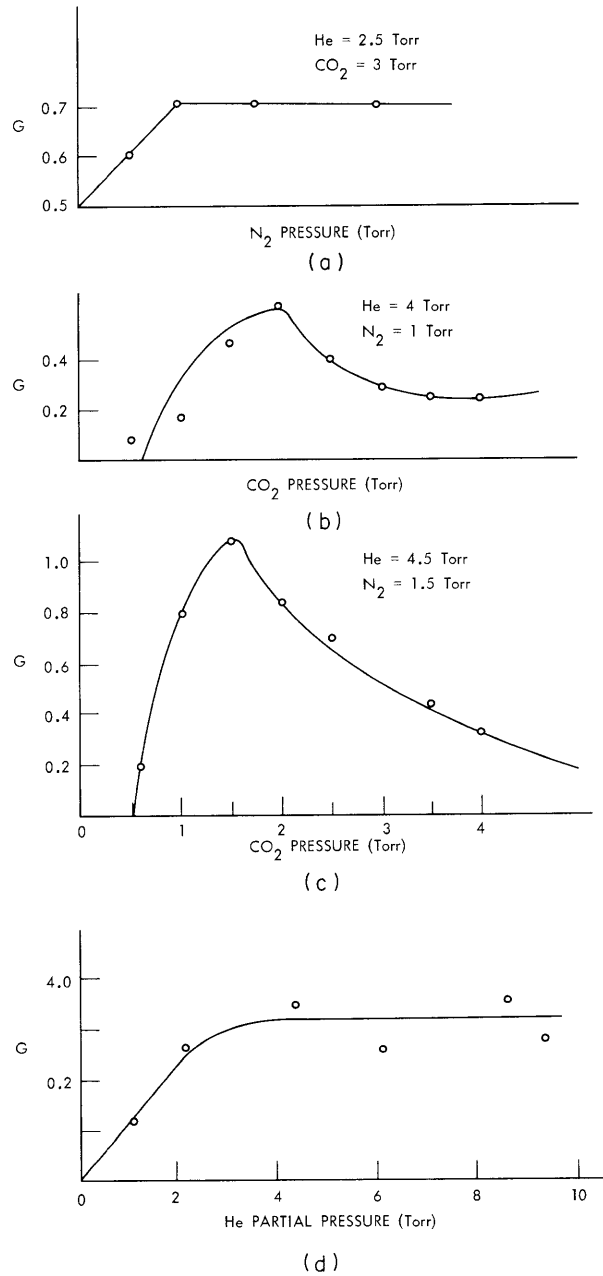


Fig. VII-19. (a) Influence of N<sub>2</sub> on the gain.  
 (b) Variation of maximum gain with CO<sub>2</sub> pressure.  
 He pressure, 4 Torr; N<sub>2</sub> pressure, 1 Torr.  
 (c) Variation of maximum gain with CO<sub>2</sub> pressure.  
 He pressure, 4.5 Torr; N<sub>2</sub> pressure, 1.5 Torr.  
 (d) Influence of He on the gain.

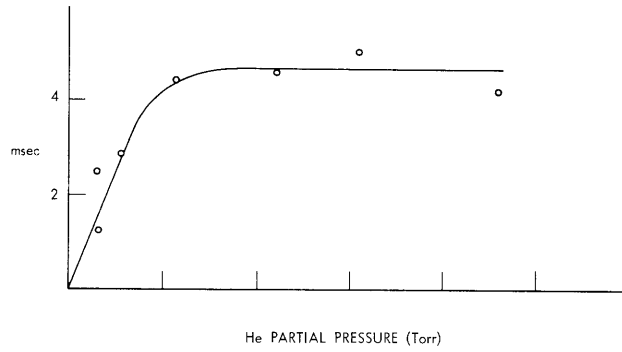


Fig. VII-20. Influence of He on the time of occurrence of maximum gain.

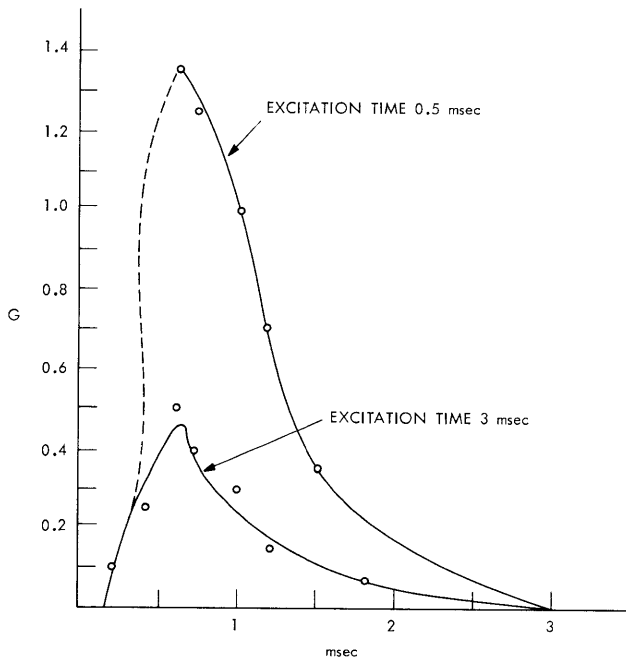


Fig. VII-21. Variation of the gain in the afterglow with  $\text{CO}_2$  pressure 2 Torr, He pressure 2.5 Torr, and  $\text{N}_2$  pressure 1 Torr.

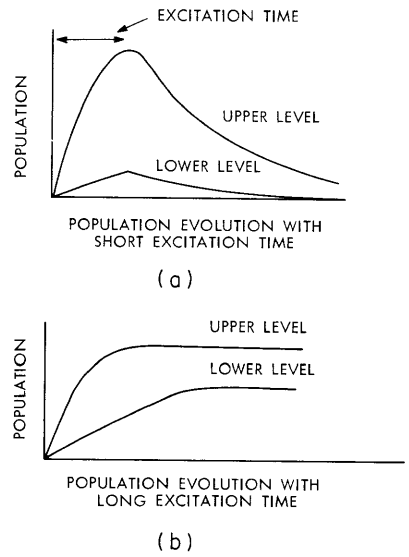


Fig. VII-22. (a) Variation of upper and lower laser levels with short excitation time. (b) Variation of the populations of lower and upper laser levels with time.

change was observed, and its importance was therefore neglected.

Figure VII-21 shows the variation of  $G$ , and the influence of the afterglow is pointed out as we also plotted in the same figure the variation of  $G$  when the excitation pulse is 3 msec. The improvement attributable to the nonexcitation of the lower level in the afterglow is a factor between 2 and 3.

### Discussion of the Results

Experimental observations show that the steady-state population inversion is reached after 3 msec excitation of the amplifier, that is, when  $G$  is too small to be observed ( $G \approx 0$ ).

Since our probe pulses are very short compared with the time constants involved in the  $\text{CO}_2$  laser,<sup>1</sup> and particularly with the relaxation time of the reaction



the gain measured is a picture of the population inversion under unsaturated conditions<sup>2</sup> of the transition  $00^{\circ}1-10^{\circ}0$ . The upper levels ( $\text{CO}_2(00^{\circ}\nu)$  with  $\nu > 1$ ) have insufficient time to relax and populate the  $00^{\circ}1$  level. Consequently, Figs. VII-17 and VII-18 are pictures of the evolution of population inversion with time.

During the excitation, two processes compete (Fig. VII-22): the buildup of the upper level through direct excitation by electron impact and resonant energy transfer with nitrogen, and the buildup of the lower level through direct excitation by electrons. At any time the population inversion is the difference between these two processes. The upper level populates faster than the lower because the gain starts increasing with time. The gain then decreases because of the buildup of the lower level. This suggests that the time constant of the decay of the gain in Figs. VII-17 and VII-18 is identical to the buildup time constant of the lower level.

Consequently, we have plotted with semi-logarithmic coordinates the decay of the gain with respect to time of Figs. VII-17 and VII-18 in Figs. VII-23 and VII-24. Figure VII-25 shows that  $\tau \times p$  is roughly constant in both cases, around  $9.0 \times 10^{-4}$  sec-Torr. The effect of helium in depleting the lower level would therefore only be to lower the saturation value.

When we use short excitation time the population inversion evolves, as shown in Fig. VII-22a, and therefore we see that we can expect a larger population inversion than in the previous case with long excitation times. Neglecting the population of the lower level in the afterglow, we can consider that the decay of the gain in the afterglow evolves as the decay of the upper laser level. Figure VII-26 shows clearly that, since the decay is a straight line in semi-logarithmic coordinates, a time constant of  $6.18 \times 10^{-4}$  sec is indicated. This time constant is very dependent on the partial He and  $\text{N}_2$  pressures,

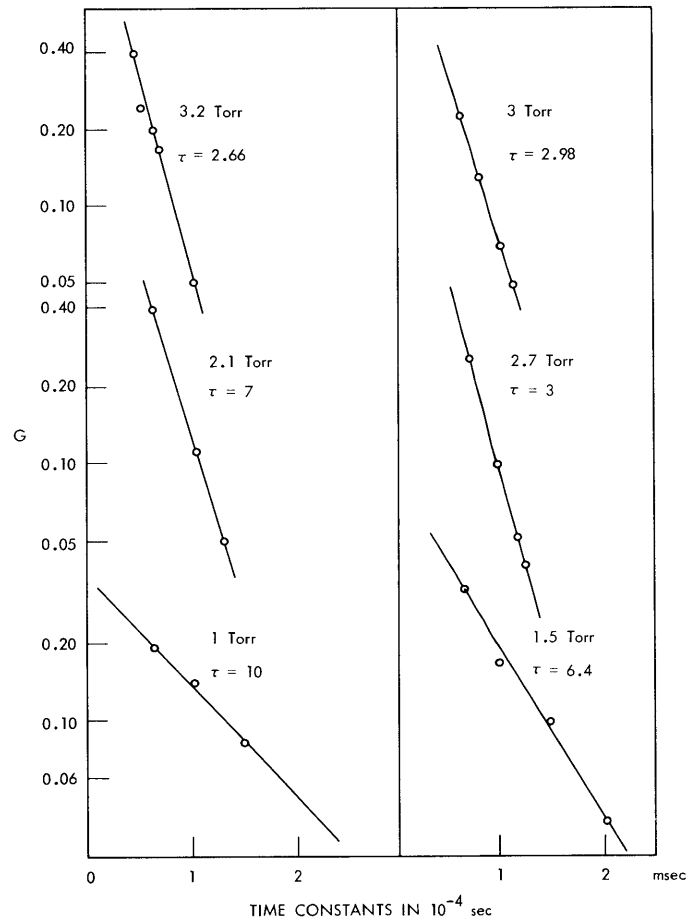


Fig. VII-23. Semi-log graph of gain decay. He pressure, 4 Torr;  $N_2$  pressure, 1 Torr.

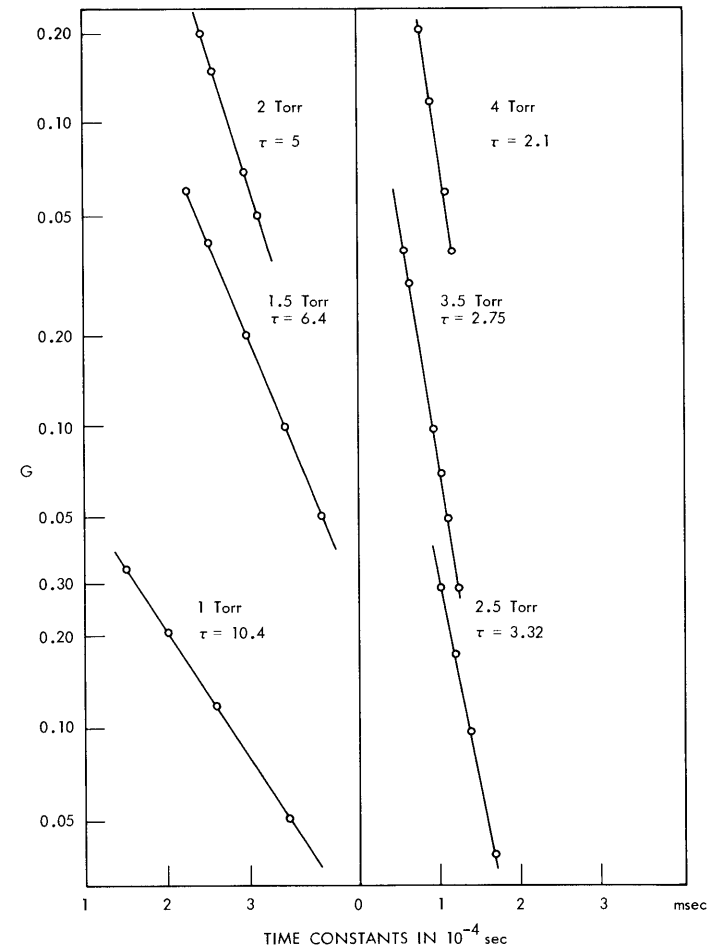


Fig. VII-24. Semi-log graph of gain decay. He pressure, 2.5 Torr;  $N_2$  pressure, 1 Torr.



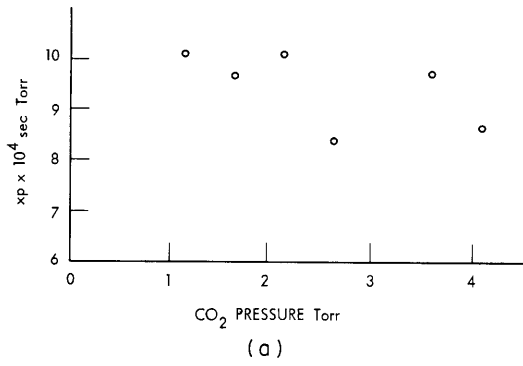
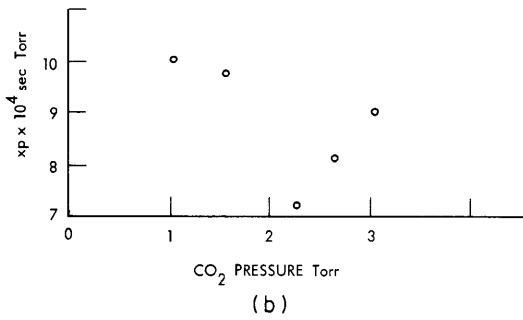


Fig. VII-25. (a)  $\tau \times p$  for the upper level buildup with He pressure 4.5 Torr, and N<sub>2</sub> pressure 1.5 Torr.



(b)  $\tau \times p$  for the lower level buildup with He pressure 4 Torr, and N<sub>2</sub> pressure 1 Torr.

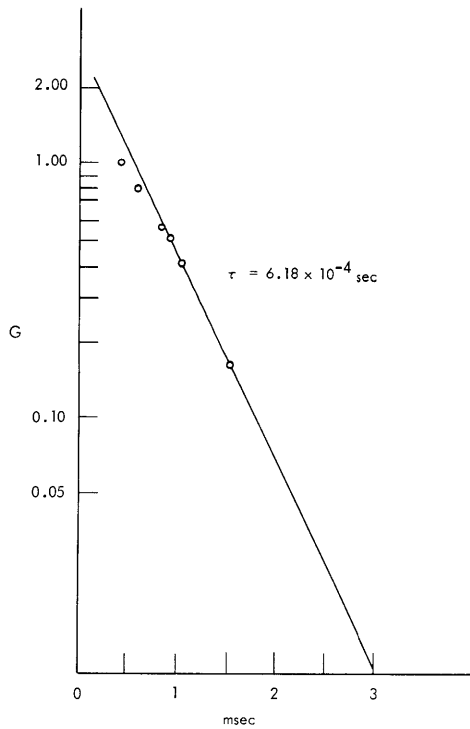


Fig. VII-26. Decay of the upper level. He pressure, 4 Torr; N<sub>2</sub> pressure, 1.5 Torr.

## (VII. APPLIED PLASMA RESEARCH)

but our data are insufficient to draw a quantitative conclusion.

We could estimate<sup>3</sup> the population inversion<sup>4</sup> to be obtained at the maximum gain as approximately  $4 \times 10^{13} \text{ cm}^{-3}$ , and the excitation time to be approximately  $18 \times 10^{-5} \text{ sec}$ , under the assumption that the upper level degenerates into 22 vibrational levels.<sup>1</sup>

### Conclusion

The gain in the glow first increases rapidly with time to achieve its maximum around 0.5-1 msec, depending on the gas mixture, and then decays to its steady-state value after 2-3 msec.

The gain in the afterglow appears to be larger than it is in the glow, and we obtain a gain up to  $2.4 \text{ m}^{-1}$ . It seems, therefore, that the most efficient way to use a Q-switched  $\text{CO}_2$  laser is to excite it by square pulses approximately 0.5 msec long.

M. A. Lecomte, L. M. Lidsky

### References

1. A. A. Offenberger, Ph.D. Thesis, Department of Nuclear Engineering, M.I.T., 1967.
2. A. Levine, Lasers, Vol. II (M. Dekker, New York, 1967), pp. 109-110.
3. A. Yariv and J. P. Gordon, "The Laser," Proc. IEEE 51, 4-29 (1963).
4. M. A. Lecomte, S.M. Thesis, Department of Nuclear Engineering, M.I.T., 1969.